## PAPER

Check for updates

# Fabrication and characterisation of a silicon-borosilicate glass microfluidic device for synchrotron-based hard X-ray spectroscopy studies

Pushparani Micheal Raj, [ID] *[a] Laurent Barbe,[b] Martin Andersson, [ID] [b] Milena De Albuquerque Moreira, [ID] [b] Dörthe Haase,[a] James Wootton,[a] Susan Nehzati,[a] Ann E. Terry,[a] Ross J. Friel [ID] [c] Maria Tenje [ID] [b] and Kajsa G. V. Sigfridsson Clauss [ID] *[a]

Some of the most fundamental chemical building blocks of life on Earth are the metal elements. X-ray absorption spectroscopy (XAS) is an element-specific technique that can analyse the local atomic and electronic structure of, for example, the active sites in catalysts and energy materials and allow the metal sites in biological samples to be identified and understood. A microfluidic device capable of withstanding the intense hard X-ray beams of a 4th generation synchrotron and harsh chemical sample conditions is presented in this work. The device is evaluated at the $K$-edges of iron and bromine and the $L_3$-edge of lead, in both transmission and fluorescence mode detection and in a wide range of sample concentrations, as low as 0.001 M. The device is fabricated in silicon and glass with plasma etched microchannels defined in the silicon wafer before anodic bonding of the glass wafer into a complete device. The device is supported with a well-designed printed chip holder that made the microfluidic device portable and easy to handle. The chip holder plays a pivotal role in mounting the delicate microfluidic device on the beamline stage. Testing validated that the device was sufficiently robust to contain and flow through harsh acids and toxic samples. There was also no significant radiation damage to the device observed, despite focusing with intense X-ray beams for multiple hours. The quality of X-ray spectra collected is comparable to that from standard methods; hence we present a robust microfluidic device to analyse liquid samples using synchrotron XAS.

## Introduction

Microfluidics has emerged as an easily adaptable platform in many research fields such as biology, medicine, marine science, geology, fossil fuels and space science.[1–4] It is possible to integrate the microfluidic platform into various applications by carefully assessing the characteristics alongside study requirements. The microfluidic technology benefits have been lauded many times in the literature; low volumes, ease of fabrication and a high degree of integration, making it attractive for adoption in various research areas. In addition, any microfluidic system is highly controllable in attributes such as ambience, flow rates and delivery patterns, *e.g.*, laminar flow, droplets or flow focusing. The highly interdisciplinary approach to microfluidics also attracts multiple fields, of which X-ray studies are gaining momentum.[5,6]

The high brilliance synchrotron light facilities worldwide provide high-intensity X-ray beams to determine the molecular structure, fingerprinting and study of many previously invisible dynamics and interactions lying in multiple layers of an atom.[7] Synchrotron facilities offer X-rays in a wide range of energies (from a few hundred eV to tens of keV), and the energy matches orbitals of the atoms (ionising radiation). The radiation interacts with matter (transmitted, scattered or absorbed). It is used to study samples in all physical forms from gas, liquid and solid (crystalline as well as amorphous) using a range of X-ray techniques (scattering, diffraction, 2D–3D-imaging and spectroscopy). However, in addition to providing spatial and/or structural and electronic information, the ionising X-ray beam can damage the samples during analysis. Water-containing samples are sensitive to X-ray induced radiolysis of the water, which forms both gas (bubbles) and aqueous free electrons, that readily reduce high valence metal ions (radiation-induced reduction). For a liquid sample, this effect can be avoided/

*[a]MAX IV Laboratory, Lund University, Lund, Sweden. E-mail: pushpa.micheal@gmail.com*

*[b]Dept. Materials Science and Engineering, Science for Life Laboratory, Uppsala University, Uppsala, Sweden*

*[c]School of Information Technology, Halmstad University, Halmstad, Sweden*

minimised by continuously exposing a fresh sample to the beam by, for example, using a flow cell.

X-ray spectroscopic techniques are based on the photoelectric effect where an inner shell electron absorbs the X-ray, and the photoelectron is ejected from the atom creating a core hole. X-ray absorption spectroscopy (XAS) is an element-specific probe to determine the local atomic and/or electronic structure of matter. It has been a key tool to collect spectroscopic information about atomic energy level structure for decades. This information is obtained by tuning the X-ray photon beam energy to match the core electron excitation energy range. The edges possibly determined are $K$-, $L$- and $M$-, named by which core electron is excited (quantum numbers $n = 1$, 2 and 3 correspond to $K$-, $L$- and $M$-edges, respectively).[8] The broad range of the X-ray sources' tunability makes this synchrotron-based analyses a powerful tool to determine oscillatory structure above the absorption edge, furnishing information about interatomic distances, near neighbour coordination numbers and *e.g.*, identity. This is provided by Extended X-ray Absorption Fine Structure (EXAFS).

Similarly, X-ray Absorption Near Edge Structure (XANES) gives information on the unoccupied valence orbitals, oxidation state, and coordination geometry (bond angles). Thus, it is compelling to combine the best of microfluidics and X-ray spectroscopy; so that one may study samples without damaging and whilst consuming low sample quantities (typically a few tens to hundreds of microliters). The small footprint and modular nature of a microfluidic platform eases integration into the X-ray detecting setup and can meet requirements such as, for example, glove box containment, which reduces the risk of exposure to hazardous samples. Thus, microfluidics are potentially invaluable when combined with analytical methods like synchrotrons or X-ray Free-Electron Lasers (XFELs). Several microfluidic devices are presented in the literature for various studies involving diffraction, small-angle scattering, serial crystallography and others.[9–12] Successful experimentation and data collections for protein structure determination, protein crystallisation,[13] studies on hydrated cells, characterisation of cells,[9] production of hexosomes,[14] and other *in situ* studies[15–17] have been reported. The devices have widely been used in scattering and diffraction studies using synchrotron facilities. Microfluidic devices used for analysing liquids using XAS reported in literature are limited to specific applications, such as vacuum studies,[18] soft X-ray XAS (energy range 0.1–1 keV)[19] or hard XAS (>1 keV) at lower energy levels (*e.g.* 4 keV).[20]

The microfluidic device reported here permits continuous screening and determination of the $K$-edge (and $L$-edges) of various metals in solutions at different concentrations and allows atomic structure determination of the metal of interest. The main challenge was to create a microfluidic chip capable of handling fluids with negligible sample damage and deposition of exposed material on the microchannel walls during beam scans over the same position for extended experiment durations. Optical transparency was considered a significant asset to view the sample movement during the X-ray scans through a visible light camera integrated into the beamline sample stage. Without this feature, it is not easy to confirm the correct sample flow through the device. The device presented here has high potential to be used for various hard X-ray absorption spectroscopy studies, as the materials used are X-ray robust, biocompatible and chemically compatible with several substances. The energy range in the synchrotron facilities is high and tuned to specific energies of interest. The SiG device performed with full functionality for more than 24 h of data collection. X-ray transparent materials are not well suited to the microfluidic chip processing as they do not etch well and so glass is superior in this instance for channel accuracy and thereby, microfluidic device discussed here could be a satisfactory alternative to study chemicals, metalloproteins, cells, *etc.*, with a high energy source like synchrotron.

Microfluidic platforms are fabricated using various materials such as paper, thermoplastics, hydrogels, silicon, and glass. The materials' surface properties are vital in choosing the appropriate one for the application.[12,17,21,22] Hence, material choice is considered vital in any microfluidic research based on the experimental method and samples involved. The microfabrication technique is also a dominant consideration for spectroscopy techniques, such as XAS, as the surface is required to be smooth to avoid/reduce any undesirable scattering effects from a materials surface roughness.[23] The material and fabrication technique considerations needed for the XAS analysis method led to the present work. A silicon–glass plasma-etched and anodically bonded microfluidic device to flow samples and study sample behaviours by interacting with high energy X-rays was developed and validated in this work.

## Experimental section

### Materials and methods

The glass–silicon–glass (SiG) microfluidic device comprises three layers, where an etched silicon wafer was sandwiched between two glass layers. The device was fabricated from borosilicate glass (referred to in the article as glass) and silicon wafers, purchased from MicroChemicals, Germany. Capillaries made of fused silica of 75 μm inner diameter (ID) and 150 μm outer diameter (OD) were purchased from Polymicro Technologies (Sweden). Polytetrafluoroethylene (PTFE) tubing of 1/16″ OD and 1/32″ ID was purchased from Elveflow, France. UV curable adhesive NOA81 (Norland Products, APM Technica, Germany) was used to bond together the silica capillaries with the SiG chip.

### Microfluidic device fabrication

The chip was designed using computer-aided-design (CAD) software (SolidWorks 2018, Dassault Systèmes, France). A Czochralski Silicon (CZ-Si) wafer (4 inches, double-sided polished, 525 μm thick, high resistivity) was first cleaned using an $N_2:O_2$ plasma (Tepla 300, Tepla) at 100 W for 5 min. This was followed by sputter deposition (Von Ardenne, CS730S) at 1000 W, producing a 250 nm thick Al thin film on both sides of the wafer. On one side of the wafer, a 1 μm thick resist layer (1813S, Shipley) was deposited by spin coating and subsequent soft bake at 115 °C. This was then exposed and developed using UV

lithography to form the microchannel resist pattern on the Al film. To transfer the pattern into the Si wafer, the Al film and Si were dry-etched (SLR, PlasmaTherm). First, the top Al film with resist was etched (RF power 800 W, using 26 sccm $Cl_2$ and 50 sccm $BCl_3$). The Al thin film acted both as hard mask (front side layer) and etch stop (back side layer) for the subsequent through-wafer dry etching of the Si wafer, which was done using the DRIE Bosch process (RF power 900 W, deposition using 30 sccm $C_4F_8$, etching using 50–90 sccm $SF_6$). Following this, the residual resist was removed by $O_2$ plasma (Tepla 300, Tepla) at 1000 W for 20 min, the Al thin film was stripped by a wet etchant (80 $H_3PO_4$ : 5 $HNO_3$ : 5 HAc : 10 $H_2O$), and the wafer was cleaned using RCA 1 (1 $NH_4OH$ : 1 $H_2O_2$ : 5 $H_2O$) and RCA 2 (1 HCl : 1 $H_2O_2$ : 5 $H_2O$). Before the wafer could be bonded to the glass cover layer, it was submerged in 1 HF : 4 $H_2O$ for 1 min, and borosilicate glass wafers (Borofloat 33, double-sided polished, 175 μm thickness) were cleaned in a 1000 W $O_2$ plasma (Tepla 300, Tepla) followed by 70 °C concentrated $HNO_3$ for 10 min. All wafers were extensively rinsed in DI water and dried by $N_2$. This was followed by preheating the wafers to 380 °C and bonding using an in-house anodic bonder, operating at a potential of 900 V.[12] Following this, the bonded wafer stack was diced (Disco, DAD 361) into the individual microfluidic devices. Each diced chip contains three independent channels, 60 mm in length 250 μm in width and 525 μm in depth. The resulting SiG microfluidic device with three parallel microchannels is 60 mm in length, 4.5 mm in width and 875 μm in depth.

Once the layers were bonded tightly, the inlets and outlets were connected to fused silica capillaries and PTFE tubing. The active microfluidic system has two kinds of fluidic resistances – external (tubing and fittings) and internal (resistance created within the channel design).[24] External resistance is a powerful tool to enhance system performance and adjust flow control. In this device, a fused silica capillary of relatively smaller diameter was intentionally connected to the SiG chip to increase the entire system's fluidic resistance (eqn (1) and (2)[25]). Different capillary and chip lengths were tested to identify appropriate fluidic resistance and flow rate. It was efficient to modify the external resistance through the capillary length, and hence the desired flow rate of >40 μl min$^{-1}$ was obtained using a channel and capillary length of 60 mm and 20 mm, respectively. The chip was tested to withstand a continuous flow using a pressure range between 10 mbar and 2 bar (the controller system capability allowed a 2 bar maximum pressure at the channel outlet). Using the Hagen–Poiseuille's law[25] and given the channel width $w$, height $h$, length of the channel section $l$, diameter $d$ and the viscosity of the fluid flowing $\eta$:

$$\text{Fluidic resistance of SiG rectangular chip} = \frac{12\eta l}{wh^3} \quad (1)$$

$$\text{Fluidic resistance of capillary} = \frac{128\eta l}{\pi d^4} \quad (2)$$

The fluid flow in the chip was monitored and controlled externally by a pressure controller (OB1 – MK3+ with four channel outlets from Elveflow, France) and a flow sensor (Microfluidic Flow Sensor (MFS) from Elveflow, France). The pressure controller was connected to 3 bar $N_2$ gas with constant pressurised gas supplied *via* standard laboratory gas lines. The channel features were visualised under a customised microscope (Nikon Eclipse Ci – NIS-Elements BR 5.21.01) to imitate the chips' position at the beamline; thus, the devices were mounted horizontally to the perpendicular direction of the beam.

Plasma etching creates a very smooth surface for channels that are less likely to disturb the desired laminar flow. The surface smoothness and dicing quality were confirmed using optical microscope imaging. The channel walls were free of any residues from the fabrication process, so there was no potential blockage of fluid flow (Fig. 2). For spectroscopic techniques, the path length (distance travelled by the X-rays through the sample medium) is an essential consideration to exploit the maximum X-ray scattering intensity.[26,27] Increased path lengths are a consequence of wider and deeper channels, which leads to an increased sample consumption rate. Thus, appropriate calculations are made to attain optimal path length *via* the dimensions of the microchannels. The beam size should also be smaller than the exposed channel to avoid 'undesired' scattering from the channel edges.[28] Beam to channel edge interaction may also result in sample deposition to the channel walls and/or device damage.

All the samples used in this study worked well at ambient temperature with no external control system for temperature or humidity or $CO_2$, and thus no specific arrangement was made for the microenvironment of the samples.

## Chip holder for SiG microfluidic devices

In microfluidic experiments involving hard X-rays at synchrotron facilities, one of the vital components for microfluidic setup is the chip holder. This is due to the fact that the microfluidic devices are mounted horizontally or vertically to the stage and the experiments are conducted in this manner for more than 24 hours. Hence, devices that are prone to fatigue or bending stresses (like the SiG device mentioned in this paper), need a robust support and clear isolation from the macroworld.

Considering the beam and beamline requirements at Balder, MAX IV, a chip holder was developed that provides strong support to side connect fluidic holders and avoid any strain on the inlet and outlet of the microfluidic device (Fig. 1). The side connects are placed at an angle with respect to the hexapod arrangement at Balder and thereby providing efficient data collection in fluorescence mode. The chip holder is compatible with the SiG device presented in this paper. The chip holder has a larger open section to ensure minimal X-ray beam impedance and make it easier to perform online and offline setup. The chip holder incorporates guided capillary paths, that prevents cracking of the junctions between the capillary and the chip.

The design was developed using SolidWorks software and fabricated using a Fused Deposition Modelling (FDM) 3D Printer with Acrylonitrile Butadiene Styrene (ABS) filament. The chip holder was made as multiple parts and glued together as a single piece. The SiG chip was removable and clamped in
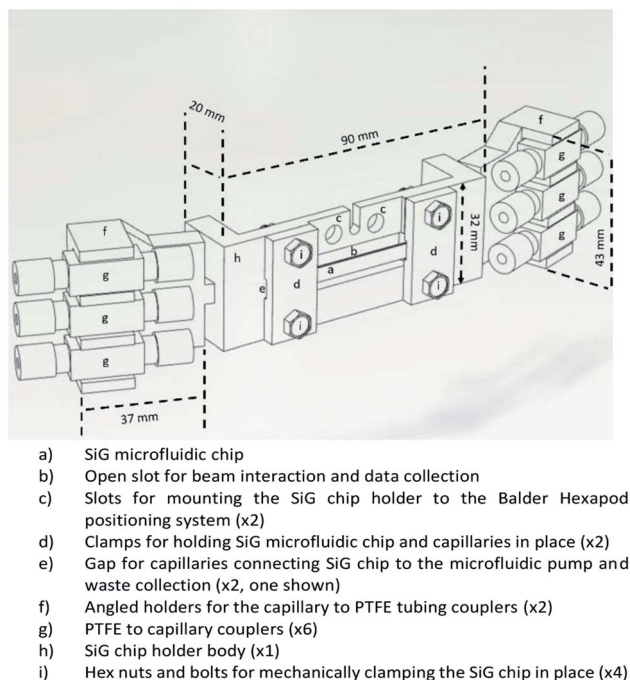
a) SiG microfluidic chip
b) Open slot for beam interaction and data collection
c) Slots for mounting the SiG chip holder to the Balder Hexapod positioning system (x2)
d) Clamps for holding SiG microfluidic chip and capillaries in place (x2)
e) Gap for capillaries connecting SiG chip to the microfluidic pump and waste collection (x2, one shown)
f) Angled holders for the capillary to PTFE tubing couplers (x2)
g) PTFE to capillary couplers (x6)
h) SiG chip holder body (x1)
i) Hex nuts and bolts for mechanically clamping the SiG chip in place (x4)

**Fig. 1** CAD image of the chip holder that supports the SiG chip mounting and angled coupling holders to prevent strain on the chip and fixings during usage.

place by the two chip clamps (Fig. 1d) and four hex nuts and bolts (Fig. 1i).

## XAS beamline set up for microfluidics

The Balder beamline at the MAX IV Laboratory synchrotron facility[29] was set up for the microfluidic flow cell experiments. The XAS experiment uses ionisation chambers (IC) to detect the incoming beam intensity ($I_0$) and the transmitted beam intensity after the sample ($I_1$), as depicted in Fig. 2a. In order to have a well-defined beam spot, a set of slits (movable apertures) were mounted in front of the sample with an additional IC detector after the slits ($I_{0s}$), the signal from which was used for normalisation of the data (transmission data, monitoring the X-ray absorption coefficient $\mu(E) = \log(I_{0s}/I_1)$, and fluorescence data as $\mu(E)$ proportional to $I_f/I_{0s}$). The three ionisation chambers ($I_0$, $I_{0s}$, $I_1$) were filled with gas mixtures of $N_2$, Ar, He to fulfil: $I_0$ 15%, $I_{0s}$ 15% and $I_1$ 75% absorption of the beam at the three different edges (Fe and Br $K$-edges, and Pb $L_3$-edge). The fluorescence detector (7-element SDD, X-PIPS, Canberra, Mirion Technologies Inc., Meriden CT) was placed at 90° to the beam path to collect the emitted X-rays from the sample, Fig. 2a.

The sample mounting at Balder is equipped with translational stages: vertical 102 mm linear PI L-406.40SD00 is holding a hexapod (PI H-811.I2) upside down, equipped with a manual full circle rotation plate, in turn, holding the lateral 103 mm linear piezo stage (SLC-24150, SmarAct). This facilitates sample positioning at 90° (transmission mode) or 45° (fluorescence mode, Fig. 2a) to the beam path. This assembly is holding the sample mounting pins from above, with a chip holder with
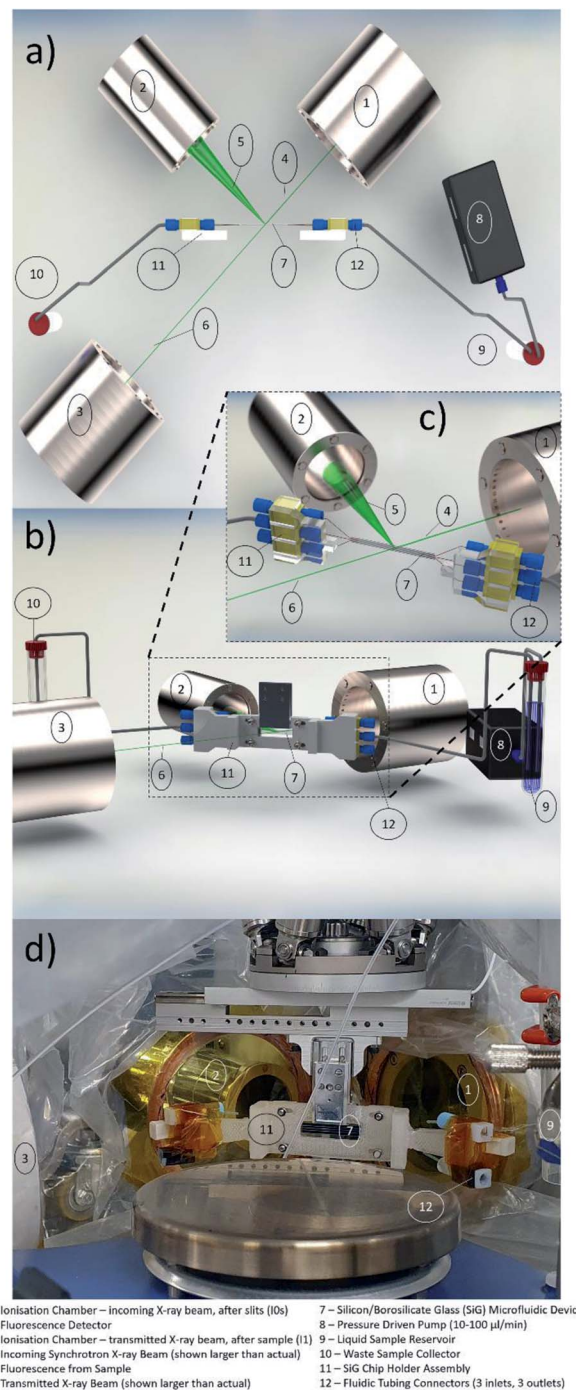


1 – Ionisation Chamber – incoming X-ray beam, after slits (I0s)
2 – Fluorescence Detector
3 – Ionisation Chamber – transmitted X-ray beam, after sample (I1)
4 – Incoming Synchrotron X-ray Beam (shown larger than actual)
5 – Fluorescence from Sample
6 – Transmitted X-ray Beam (shown larger than actual)
7 – Silicon/Borosilicate Glass (SiG) Microfluidic Device
8 – Pressure Driven Pump (10-100 μl/min)
9 – Liquid Sample Reservoir
10 – Waste Sample Collector
11 – SiG Chip Holder Assembly
12 – Fluidic Tubing Connectors (3 inlets, 3 outlets)

**Fig. 2** (a) A schematic view of the XAS microfluidic set up at the beamline; in top view detectors are the ionisation chambers ($I_{0s}$ before the sample and $I_1$ after the sample) and the fluorescence detector at 90° angle to the X-ray beam (green line). The microfluidic flow cell (SiG) is positioned at a 45° angle to the beam and fluorescence detector to optimise the signal and with the channel lateral to the table; that can be translated in X, Y and Z. (b) An isometric view of the schematic setup showing the SiG device in position within the chip holder. (c) Close up schematic view showing the SiG chip's orientation within the X-ray beam (chip holder has been removed for clarity, and X-ray beam sizes have been increased for visualisation). (d) Picture from the Balder beamline with the flow cell set up in a glove bag with Kapton® foil (low X-ray background signal) "windows" facing detectors (fluorescence, $I_{0s}$ and $I_1$). The SiG chip is mounted in a chip holder hanging from the translation stage assembly in the beam path as depicted in schematic '(a) & (b)'. Note: all component number labels are given at the bottom of the figure.

the SiG chip mounted on the pins and secured with a metal latch (Fig. 2d). The chip holder supports the inlet and outlet ports for the three separate channels on each side (Fig. 2b). A small endoscope microscope (Supereyes N015-2) is mounted facing the sample (when in 45°) for visual sample alignment to the beam with in-house software, Orthoviewer (not shown).

The SiG device was utilised to flow samples with an element of interest at >13 keV X-ray energy (atomic number 31 and above). Some of these elements, especially in combination with organic solvents have potentially increased toxicity and hazard levels. Thus, a moderate-risk glove bag was prepared around the entire setup that covered the chip, connectors, flow sensors, and reservoirs, including waste, to avoid any splashing of potentially hazardous liquids on the detectors and chambers (see Fig. 2d). The glove bag had appropriate Kapton® (polyimide, low X-ray background material) windows on the beam path and fluorescence detector side to withstand the beam and reduce unwanted X-ray signals to a minimum, see Fig. 2d.

A requirement of high importance was the flow rate control, as lower flow rates might result in constrained sample replenishment and therefore radiation damage of the sample because of prolonged exposure (in the range of millisecond) to the beam. To control the sample flow through the SiG device, a pressure-driven OB1 Elveflow controller (MK3, Elvesys, France) was placed on the experimental table and connected to the sample reservoir. The device was optimised to have a flow rate range from 40 μl min$^{-1}$ to 1200 μl min$^{-1}$, which assured sample replenishment required for the beam characteristics, determined based on tests conducted off-beamline and beamline. The fluid flow was remotely controlled outside the beamline hutch (the hutch door is interlocked during X-ray experiments to avoid exposure to dangerous levels of ionising radiation) to start/stop the flow and continuously monitor the applied pressure and resulting flow.

### Chemicals and solutions

Ferric iron trichloride hexahydrate, Fe(III)Cl$_3$·6H$_2$O (CAS 10025-77-1) puriss from Sigma Aldrich was dissolved in Milli-Q (MQ) water to a concentration of 1 M or 0.01 M. Sodium bromide, NaBr (CAS 7647-15-6) BioUltra >99.5% from Sigma Aldrich was dissolved in MQ water to a concentration of 1, 0.1, 0.01 and 0.001 M.

Lead di(acetate) trihydrate, PbAc$_2$ (C$_4$H$_6$O$_4$Pb·3H$_2$O) (CAS 6080-56-4) from Sigma Aldrich was dissolved in MQ water to a concentration of 1 and 0.1 M. Lead dichloride, PbCl$_2$ (CAS 7758-95-4) from Sigma Aldrich was dissolved in MQ water to a concentration of 0.01 and 0.001 M. Before filling the sample reservoir in the flow set up, all solutions were degassed by ultrasonic bath and filtered through a syringe filter (cut off 2 μm) to remove air and any particles, respectively.

### X-ray data collection

XAS data were collected in fluorescence and/or transmission mode at the Balder beamline (MAX IV Laboratory synchrotron light facility, Lund University, Sweden). The LN2 cooled double crystal (Si111) monochromator (FMB Oxford, UK) was

calibrated to the first inflexion point of the Fe-foil, 7112 eV, for the iron K-edge data collection, and to the first inflexion point of the Pb-foil, 13 035 eV, for the lead L$_3$-edge and bromine K-edge data collections. The focused X-ray beam (50 × 50 μm$^2$) passed through an aperture of movable slit blades set to vertical 40 μm × horizontal 90 μm, giving the final beam dimensions. The channel of the SiG chip was aligned to the beam position by vertical scanning over the channel.

The sample solution was flowed through the fluidic channel at rates between 40 μl min$^{-1}$ to 80 μl min$^{-1}$. At an energy above the absorption edge of interest, the fluorescence counts per second were checked, and the region of interest (roi) was set around the emission line of interest (Fe Kα, Br Kα or Pb Lα). The distance between the sample and the fluorescence detector was optimised to be in the linear response range. If needed, a Z-1 filter (Mn for Fe and Se for Br/Pb) was used in front of the detector to decrease the elastic scattering peak.

Continuous fly scans[30] to record EXAFS (settings: dt 10 ms, energy step 0.25 eV, −200 to +560 eV around $E_0$, 100 s per scan) or only XANES (settings: dt 10 ms, energy step 0.2 eV, −50 to +70 eV around $E_0$, 25 s per scan) were started when the sample was confirmed in the channel by checking the increase in fluorescence count. The number of scans is indicated in each figure (Fig. 3, 5 and 6). $E_0$ in this case was the tabulated edge energy of the element (Fe K 7112 eV, Br K 13 474 eV, Pb L$_3$ 13 035 eV).

Samples were changed by changing the sample reservoir with a new solution, first water to clean the microfluidic device, and then a new sample (fluorescence counts in the roi was used
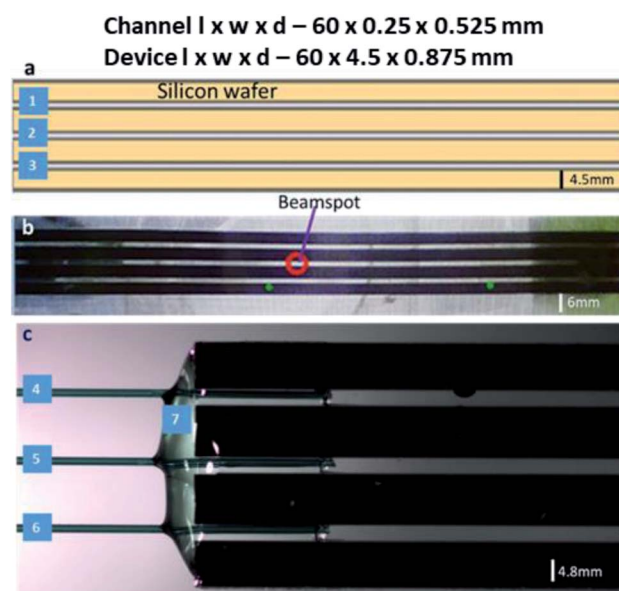


**Fig. 3** The microfluidic device and design. (a) CAD diagram of the device with alternate silicon and channel layers (1, 2 & 3); (b) final assembled device mounted on the beamline, a beam of 50 × 50 μm$^2$ size is focused on the microchannel inside the indicative red circle, which is not the actual beam but indicative of the position; (c) capillaries (4, 5 & 6) glued into the channels using epoxy (7) for flow regulation and connection of PTFE tubing.

to confirm the presence or absence of sample in the channel). Different SiG devices were used for the four different salt solutions tested, even though the SiG chip is fully reusable for the same samples after proper cleaning. Post experiment, the SiG devices were scrutinised under the microscope for any sign of radiation damage to the device material.

The multiple scan repeats of each sample solution were first examined for changes in the edge region; if no changes were observed, they were merged into an averaged spectrum. The spectrum normalisation and extraction of EXAFS oscillations and conversion of the energy scale to the wave-vector ($k$) scale were performed as previously described.[31,32] Simulation of $k^3$-weighted EXAFS ($S_0^2 = 1.0$) was done using phase functions calculated with FEFF7.[33] Fourier transforms of EXAFS spectra were calculated using in-house software and $\cos^2$ windows extending over 10% at both $k$-range ends ($k = 2.1$–$10.9$ Å$^{-1}$). $E_0$ (13 474 eV) was refined in the fit procedure to a zero-energy shift of 3.8 eV. The goodness of fit was judged by calculation of the Fourier-filtered $R$-factor ($R_F$).[32]

Demeter program,[34] Hephaestus, was used to calculate the attenuation length and transmitted fraction of X-rays through the device windows of borosilicate glass (formula $(SiO_2)_{0.9}(B_2O_3)_{0.1}$, density 2.23 g cm$^{-3}$) at the X-ray energies (edge and $K\alpha$ emission) of Fe (7.1 and 6.4 keV) and Br (13.5 and 11.9 keV). It was also used for calculations of the sample molar concentration for transmission of unit edge step.

## Results and discussion

### Microfluidic device fabrication

The SiG microfluidic device was designed with consideration of the X-ray beam requirements (beam size: 50–100 μm; photon flux $\sim 10^{11}$–$10^{12}$ photons per s) and for using various toxic and harsh samples, e.g., iron chloride, bromide salt solutions, lead acetate in aqueous solutions and perovskite solutions. Borosilicate glass was chosen as it tested to withstand hard X-ray beams at the MAX IV facility up to 13 keV energy without any window degradation. The material also has commendable optical transparency during beamline and off-beamline tests combined with microscopy analysis (Fig. 3). The device was reusable unless there are concerns of cross-contaminations due to insufficient cleaning, damage or adverse chemical reactions. In this study, the device was tested, both at off-beamline and at beamline, with samples of pH between 2 and 5, after a thorough cleaning using DI water at higher flow rates ($\sim$1500 μl min$^{-1}$) to ensure flushing away of residues from the previous experiment. Nevertheless, with the iron chloride samples, the discolouration in the glue was noted, hence, a new chip was used to overcome ageing and avoid any spillage of samples.

### Chip holder fabrication and setup

The chip holder was successfully manufactured using the FDM 3D Printer from opaque ABS filament material. This material is more durable and resistant to degradation than polylactic acid (PLA). The chip holder was made as multiple parts and glued together as a single piece (see Fig. 4).
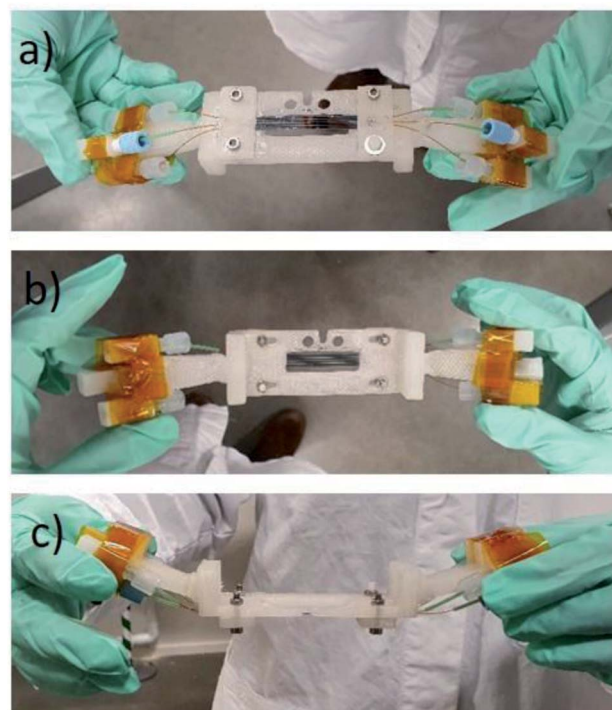


Fig. 4 The chipholder and mounted SiG chip with three connected channels. (a) Side view facing the beam and detector; (b) off-beamside view; (c) top view observing the angled holders for connectors.

The angled coupling holders were inserted to the main holder body. Chip holder was printed in parts as the main chip window and side connect holders. The angle avoided collision with other equipment during horizontal translations. The chip holder is light weight and stiff which makes the whole microfluidic set up to be portable into and out of the Balder experimental station and allows for offline setup. As the SiG devices and attaching capillaries are delicate the chip holder is a vital component in the microfluidic setup. The chip holder allows the use of three channels in parallel with different samples, potentially, being used in each.

### Material compatibility to X-ray beams

To obtain quality data through X-ray spectroscopy techniques, there are several considerations to be made with respect to beam/material interactions. When the material itself absorbs more photons, this subsequently decreases the incident and emitted beam intensities, leading to beam attenuation.[35] The second most common behaviour is the scattering effect from the material that arises due to factors such as morphologies of surface and wall roughness and thickness.[23] The glass wafers used as sealing layers on either side of the silicon wafer effectively worked as the X-ray windows and were of 175 μm thickness (Fig. 3b). Therefore, at a 45° angle to the incoming beam, there was a path length of 247.5 μm through the glass on each side of the sample material. The X-ray beam needs to pass through this window twice (total 495 μm glass) in order to be detected, either on the fluorescence detector detecting the X-ray

emission or in the $I_1$ ionisation chamber after the sample detecting the transmitted beam. Materials display a general decrease in the X-ray attenuation cross section ($\mu/\rho$) at higher X-ray energies; hence, more X-rays pass through the materials at higher energies. The X-ray compatibility of the chip's glass windows were compared at energies of Fe $K$-edge (7.1 (6.4) keV, $K$-edge transition ($K\alpha$ emission)) and Br $K$-edge (13.5 (11.9) keV, $K$-edge transition ($K\alpha$ emission)). At the lower energies, $\sim$7 keV (7.1 (6.4) keV), the glass material absorbed most of the photons; at these energies, borosilicate glass has an attenuation length of 95 (70) $\mu$m, which is defined as the distance into a material where the intensity drops to $1/e$ ($\sim$37%), and hence the 495 $\mu$m glass would transmit only 0.5–0.1%. As a result, poor spectral quality even for the concentrated 1 M FeCl$_3$(aq) solution (Fig. 4a, black spectrum) compared to the 1 M NaBr(aq) (Fig. 5b, green spectrum). The $\sim$13 keV (13.5 (11.9) keV) X-ray beam is transmitted to 32–45% through the glass (attenuation length 620 (430) $\mu$m). To summarise, the lower energy range, *e.g.*, Fe $K$-edge (7 keV), resulted in a low signal-to-noise ratio, as discussed above. Whilst the device tested to study the Br $K$-edge at 13 keV by flowing NaBr(aq) solution resulted in higher quality spectra (Fig. 5b) because the photon energy increased above the lattice interaction energy of the device and therefore, the comparably more of X-ray photons were transmitted as opposed to being absorbed, increasing the XAS signal-to-noise ratio.

The microfluidic device was visually inspected for any radiation damage (RD), as this is considered one of the most common side-effect results when operating with intense X-ray beams at synchrotron facilities. High-intensity ionising radiation can have multiple effects on materials in a relatively short time, often causing the material to physically, mechanically, optically and chemically alter or degrade.[36,37] RD provides a physical limit to X-ray analysis on certain fragile samples, materials used in sample holders and, in many cases, the duration of a test at a single local point of
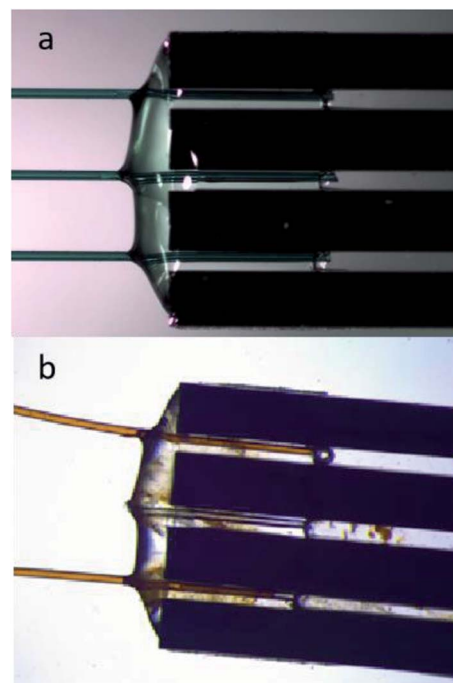


Fig. 6 Chip before and after beam exposure, to observe beam–material interaction behaviour. (a) A newly fabricated SiG chip: (b) The new SiG chip tested with FeCl$_3$(aq) samples at 7 keV, and after 24 h of testing on the same chip, a slight discolouration of the epoxy glue material was identified. However, no sample deposition or deformation of the chip's window material identified and hence reused with the same sample.

interest. Inelastic scattering converts photon energy into lattice vibrations, causing heating, which results in physical damage to the material, such as melting or deformation.[38] The results from this work show that the SiG device was able to withstand the high energies of X-ray beams at the Balder beamline and provide good optical transparency to aid correct experimental setup. The SiG chip appeared sufficiently X-ray inert, to the intense beam focused on a single position for more than 24 h to maintain full microfluidic and XAS functionality.

Post-experiments, the chip was imaged to observe any physical changes that might have occurred due to RD or any deformations or depositions to understand the result of beam–material interaction. The devices, pre- and post-experiments at beamline, were microscopically compared (Fig. 6). There was slight discolouration in the epoxy glue material at the tubing to chip junction, that has interacted with the iron chloride sample, but with little effects on device functionalities (Fig. 6b). Moreover, the SiG chip, when used with NaBr solution, resulted in no discolouration, and no other forms of damage, even when the chip was scanned and focused with an intense X-ray beam on the same spot for a longer time, *e.g.*, more than 48 h. Hence, the SiG device was successfully used as a sample delivery system for XAS experiments of higher energy ranges since no deviations physically, optically, or chemically were observed. The materials of choice, silicon, and borosilicate were chemically inert and
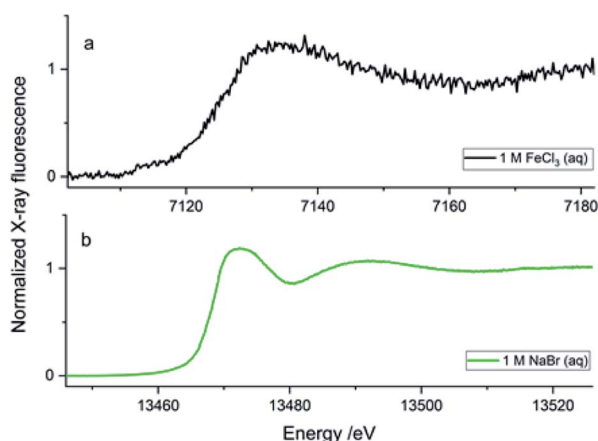


Fig. 5 Fluorescence mode detected XANES. Each presented edge spectrum is an average of 5 scans (á 25 s). (a) Fe $K$-edge measured on FeCl$_3$·6H$_2$O dissolved in water (FeCl$_3$(aq)) to the concentration of 1.0 M (black) in the SiG chip at the flow rate 10 $\mu$l min$^{-1}$. (b) Br $K$-edge measured on NaBr dissolved in water (NaBr(aq)) to the concentrations of 1.0 M (green), in the SiG chip at flow rate 40 $\mu$l min$^{-1}$.

resistive to X-rays and, therefore, optimal for use with the focused beam at prolonged exposure times with harsh, toxic, and hazardous samples at high-energy ranges.

## X-ray absorption spectroscopy of solutions

The SiG device was successfully adapted to the beamline requirements, and XAS experiments were conducted with different aqueous solutions in the higher energy range. The Pb $L_3$-edge and Br $K$-edge were probed in aqueous solutions with either $Pb^{2+}$ or $Br^-$ as the absorbing species, respectively. The purpose was to assess the quality of data and define the absorber's useful concentration range in both transmission and fluorescence mode detection of the XAS data.

In Fig. 7, the XANES scans show the rise of the edge in the $\mu(E)$ absorption coefficient, detected in fluorescence geometry (sample at 45°) by either the fluorescence detector ($I_f/I_{0s}$ – blue/ green line), or as the transmitted signal detected in $I_1$ ($\log(I_{0s}/I_1)$ – dark grey line). The properties of the SDD fluorescence detector limits fluorescence detection: too high concentrations suffer from non-linearity by the detector due to dead time in the detector elements. The deadtime problem, which suppresses the signal intensity, is handled by limiting the total photon count number hitting the detector by either moving the detector away from the sample or attenuating the signal. Too low a concentration would have a problem with the signal-to-noise ratio. As the range of concentrations was varied from 1 M to 1 mM, there is an evident decrease in the signal-to-noise ratio as the concentrations reduced. The SiG device can be used to record quality data down to 1 mM concentrations by increasing the number of scans. In Fig. 7b, each spectrum is an average of 5 scans, which easily can be increased without consuming too large sample volumes (5 scans á 25 s, at 40 μl min$^{-1}$ = 2 min would spend 80 μl).

The second problem is that the fluorescence signal's proportionality to $\mu(E)$ depends on the sample's thickness and concentration. The linear proportionality breaks down in thicker and more concentrated samples, where the penetration depth decreases while the absorption coefficient increases over the edge, resulting in fewer atoms of interest contributing to the detected signal.[39] In the absorption spectrum, structures are suppressed; for example, the white line (top of the edge) and the EXAFS oscillations; this is called self-absorption. The transmission signal is not distorted by the dead time in the fluorescence detector and would not suffer from the same self-absorption. Therefore, it would represent the "true" signal shape of the edges. However, at too low absorber concentrations, the edge step is too small to be detected. Comparing the simultaneously recorded fluorescence and transmission spectra for each concentration, an optimal detection range for the SiG device can be defined for the 13–14 keV X-rays.

The optimal concentration of the PbAc$_2$ and NaBr water solutions for a transmission sample to give an absorption edge step of ~1 can be calculated. For the SiG chip with the sample channel depth of 525 μm and an X-ray pathlength in 45° of 742 μm would the concentrations be ~1.35 M NaBr at the Br $K$-edge and ~0.69 M PbAc$_2$ at the Pb $L_3$-edge. Thus, transmission
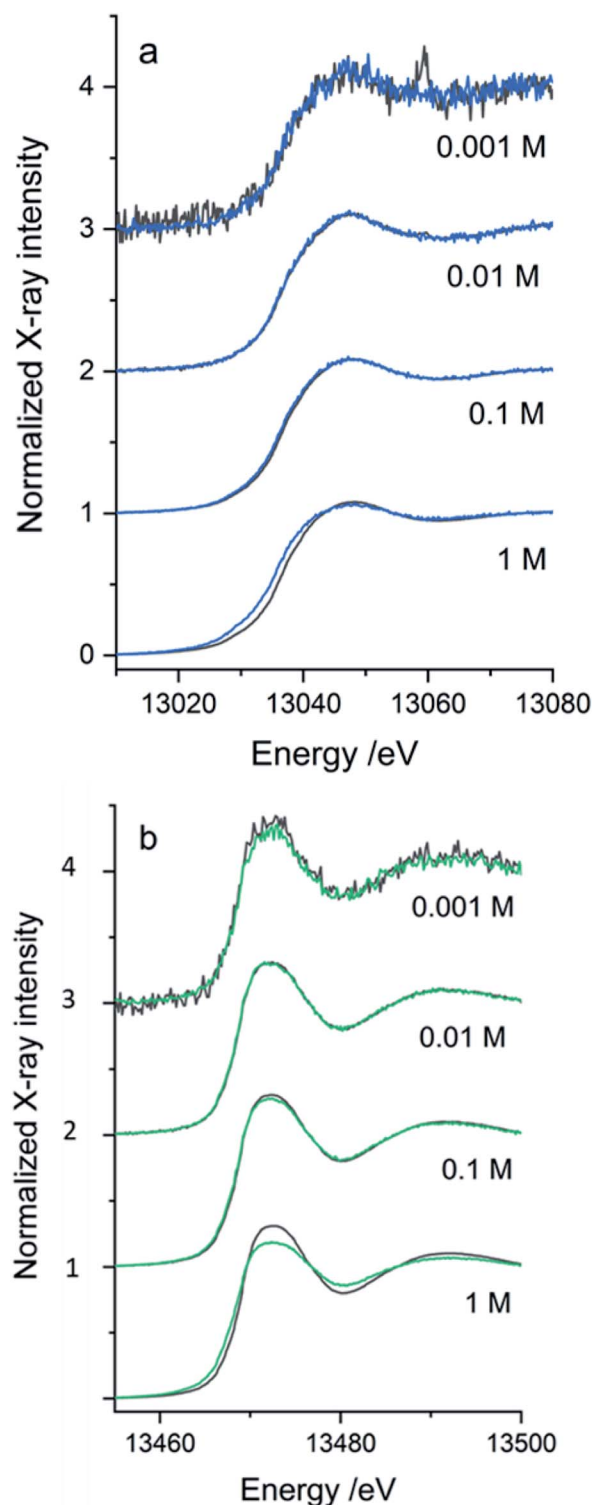


Fig. 7 XANES spectra recorded in transmission (dark grey) and fluorescence (blue/green) mode detection simultaneously on the SiG chip. (a) At the Pb $L_3$-edge on PbCl$_2$ in water solution 0.001 M and 0.01 M (each spectrum is an average of 6 scans) and on PbAc$_2$ in water solution 0.1 M and 1 M (average of 4 scans); (b) at the Br $K$-edge on NaBr in water solution 0.001–1 M concentrations (average of 5 scans).

detection is close to optimal for the 1 M samples in the SiG device. However, in the concentration range tested for the Pb $L_3$-edge, transmission detection can be used down to 10 mM, while the 1 mM spectrum is too noisy with an artefact from a monochromator crystal glitch visible as a sharp peak in Fig. 7a – top spectrum dark grey. The optimal range of fluorescence detected data would be >1 to <100 mM concentration (Fig. 7a). At 1 M the self-absorption starts to be visible as a suppressed peak in the fluorescence spectrum (blue) compared to the transmission spectrum (dark grey). At the Br $K$-edge, similar ranges apply, but the self-absorption in fluorescence is stronger and appear to some extent already in the 100 mM range and is evident in the 1 M spectrum; see Fig. 7b – bottom spectrum in green. Transmission detection was feasible down to 1 mM, even if the fluorescence spectrum, in this case, was less noisy, see Fig. 7b top spectra. The signal-to-noise ratio was overall better in the Br data set than the Pb data set (Fig. 7b versus 7a), which can be explained firstly by the fact that the fluorescence yield is higher for $K$-edge than $L$-edge (=more fluorescence generated/ absorption event). Secondly, that the ~450 eV higher excitation energy of the Br $K$-edge gave ~60 μm longer attenuation length in borosilicate glass for the incoming beam and the ~1400 eV higher emission energy (Br $K\alpha$ 11.92 keV, Pb $L\alpha$ 10.55 keV) gave ~130 μm longer attenuation length for the signal going to the fluorescence detector (=less absorption of X-rays in the SiG device glass windows for Br $K$-edge).

To obtain information on the local atomic structure around the absorbing atom, one would typically extend the energy range to include the extended X-ray absorption fine structure (EXAFS) region 50–1000 eV above the absorption edge. To evaluate the data quality for EXAFS measurements from the microfluidic device, longer energy scans were repeated ten times on the bromide solutions (total 17 min scan time). Bromide in water solution is a difficult test object since the EXAFS oscillations are rapidly dampened with very low amplitude $k > 9$ Å$^{-1}$.[40,41] The week oscillations at higher $k$ will suffer

significantly from noise. In the concentration series, the 1 and 0.1 M solutions gave good enough EXAFS data in transmission after 10 scans (Fig. 7a) to attempt to fit a simple model of one oxygen shell (Br–O) simulating the coordinating water molecules around the bromide. In the Fourier transform of EXAFS (Fig. 8b), only one main peak is visible around the reduced distance of 2.7 Å, indicating one main distance of the coordinating waters. A best fit was achieved for both concentrations when fixing the Br–O coordination number to 8 and let the interatomic distance ($R$) and Debye-Waller factor ($\sigma^2$) be fitted to ~3.25 Å and ~0.026 Å$^2$, respectively, see the green lines in Fig. 8. In the aqueous NaBr solution, each Br$^-$ would then be surrounded by ~8 water molecules at a distance of ~3.25 Å, which is in good agreement with literature data on aqueous RbBr solution[40] (8–10 water at ~3.26 Å from EXAFS and MXAN analysis). By increasing the number of scans, the signal-to-noise could, of course, be improved, but in this case, it would also increase the sample consumption in the fluidic setup.

## Conclusion

The SiG microfluidic device presented here will allow a continuous XAS analysis of liquid samples using X-ray beams of higher energies above 13 keV. The device fabrication uses a relatively rapid and scalable manufacturing protocol to obtain parallel channels in the single SiG chip that has been proven that good XAS data can be obtained with this device over a long experimental time period, typical of synchrotron-based hard XAS experiments. The capillary connections on either side of the glass–silicon–glass chip offer tuning opportunities of the fluidic resistance, thereby providing the required flow rate to avoid any radiation damage when using high-intensity X-ray beams. Regular sample replenishment in the region of interest results in negligible damage to the sample, thereby avoiding any deposition of samples on the channel walls. The choice of material (borosilicate windows) helped to focus beams of higher energies (13 keV and above) at a specific point for a longer time coupled with broad optical transparency. Optical transparency is essential for techniques involving synchrotrons as this allows for visual inspection of device performance via remote imaging as no physical inspection during operation, due to high levels of X-ray radiation, is permitted. The whole microfluidic platform is highly portable and easily mounted in the beamline hutch. Post-experiment cleaning proves to be effective, and this helps in device reusability for the same samples. The device provides flexibility, simplicity, optical transparency and optimal attenuation characteristics, particularly for >13 keV and the path length is optimal for absorber concentrations 1–0.1 M in transmission XAS, and can be used down to 1 mM in fluorescence.

Further research with this microfluidic setup is being carried out with a wider range of samples and integration of the device with additional analysis techniques. As a robust, well-characterised system, this platform opens capabilities to seek answers to novel scientific questions at synchrotron light sources.
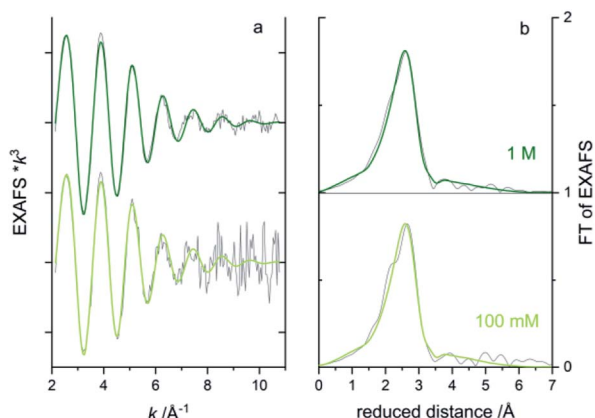


**Fig. 8** Br $K$-edge EXAFS of NaBr in water solution 1 M (dark green) and 100 mM (light green), each spectrum is an average of 10 scans (giving total scan time ~ 17 min per average spectrum). (a) The $k^3$ weighted extracted EXAFS oscillations experimental data (grey) and fitted model with 8 oxygen scatterers (green); (b) the Fourier transform of EXAFS in region $k$ 2.1–10.9 Å$^{-1}$, same colour code as in (a).

## Conflicts of interest

There are no conflicts to declare.

## Acknowledgements

## References

1 X. Luo, P. Su, W. Zhang and C. L. Raston, Microfluidic Devices in Fabricating Nano or Micromaterials for Biomedical Applications, *Adv. Mater. Technol.*, 2019, **4**(12), 1900488.

2 J. Gao, S. Nair, M. H. G. Duits, C. Otto and F. Mugele, Combined microfluidics–confocal Raman microscopy platform for studying enhanced oil recovery mechanisms, *J. Raman Spectrosc.*, 2019, **50**(7), 996–1007.

3 A. Aryasomayajula, P. Bayat, P. Rezai and P. R. Selvaganapathy, Microfluidic Devices and Their Applications, in *Springer Handbook of Nanotechnology*, ed. B. Bhushan, Springer Berlin Heidelberg, Berlin, Heidelberg, 2017, pp. 487–536.

4 J. El-Ali, P. K. Sorger and K. F. Jensen, Cells on chips, *Nature*, 2006, **442**, 403–411.

5 D. C. F. Monteiro, D. von Stetten, C. Stohrer, M. Sans, A. R. Pearson, G. Santoni, P. van der Linden and M. Trebbin, 3D-MiXD: 3D-printed X-ray-compatible microfluidic devices for rapid, low-consumption serial synchrotron crystallography data collection in flow, *IUCrJ*, 2020, **7**(2), 207–219.

6 P. Micheal Raj and I. Valpapuram, Automated, Controlled and Portable Mini Incubator for Passive Microfluidic Platforms in Biological Applications, *Int. J. Sci. Eng. Appl. Sci.*, 2020, **6**(11), 93–102.

7 E. P. Bertin, *Principles and Practice of X-Ray Spectrometric Analysis, Book Chapter 5*, 1975, ISBN 978-1-4613-4416-2.

8 M. Newville, Fundamentals of XAFS, *Rev. Mineral. Geochem.*, 2014, **78**(1), 33–74.

9 A. Ghazal, J. P. Lafleur, K. Mortensen, J. P. Kutter, L. Arleth and G. V. Jensen, Recent advances in X-ray compatible microfluidics for applications in soft materials and life sciences, *Lab Chip*, 2016, **16**(22), 4263–4295.

10 S. Guha, S. L. Perry, A. S. Pawate and P. J. A. Kenis, Fabrication of X-ray compatible microfluidic platforms for protein crystallisation, *Sens. Actuators, B*, 2012, **174**, 1–9.

11 B. Weinhausen and S. Koster, Microfluidic devices for X-ray studies on hydrated cells, *Lab Chip*, 2013, **13**(2), 212–215.

12 T. Beuvier, E. A. Panduro, P. Kwasniewski, S. Marre, C. Lecoutre, Y. Garrabos, C. Aymonier, B. Calvignac and A. Gibaud, Implementation of *in situ* SAXS/WAXS characterisation into silicon/glass microreactors, *Lab Chip*, 2015, **15**(9), 2002–2008.

13 D. S. Khvostichenko, J. M. Schieferstein, A. S. Pawate, P. D. Laible and P. J. A. Kenis, X-ray Transparent Microfluidic Chip for Mesophase-Based Crystallisation of Membrane Proteins and On-Chip Structure Determination, *Cryst. Growth Des.*, 2014, **14**(10), 4886–4890.

14 A. Yaghmur, A. Ghazal, R. Ghazal, M. Dimaki and W. E. Svendsen, A hydrodynamic flow focusing microfluidic device for the continuous production of hexosomes based on docosahexaenoic acid monoglyceride, *Phys. Chem. Chem. Phys.*, 2019, **21**(24), 13005–13013.

15 Y. Gicquel, R. Schubert, S. Kapis, G. Bourenkov, T. Schneider, M. Perbandt, C. Betzel, H. N. Chapman and M. Heymann, Microfluidic Chips for *In Situ* Crystal X-ray Diffraction and *In Situ* Dynamic Light Scattering for Serial Crystallography, *J. Visualized Exp.*, 2018, **134**, 57133.

16 M. Herbst, E. Hofmann and S. Förster, Nucleation and Growth Kinetics of ZnO Nanoparticles Studied by *in Situ* Microfluidic SAXS/WAXS/UV-Vis Experiments, *Langmuir*, 2019, **35**(36), 11702–11709.

17 T. Lange, S. Charton, T. Bizien, F. Testard and F. Malloggi, OSTE+ for *in situ* SAXS analysis with droplet microfluidic devices, *Lab Chip*, 2020, **20**(16), 2990–3000.

18 J. Zheng, W. Zhang, F. Wang and X.-Y. Yu, Enabling liquid solvent structure analysis using hard X-ray absorption spectroscopy with a transferrable microfluidic reactor, *J. Phys.: Condens. Matter*, 2018, **30**(18), 18LT01.

19 M. Nagasaka, H. Yuzawa, N. Takada, M. Aoyama, E. Ruhl and N. Kosugi, Laminar flow in microfluidics investigated by spatially-resolved soft X-ray absorption and infrared spectroscopy, *J. Chem. Phys.*, 2019, **151**(11), 114201.

20 J. Probst, C. N. Borca, M. A. Newton, J. van Bokhoven, T. Huthwelker, S. Stavrakis and A. deMello, *In Situ* X-ray Absorption Spectroscopy and Droplet-Based Microfluidics: An Analysis of Calcium Carbonate Precipitation, *ACS Meas. Sci. Au*, 2021, **1**(1), 27–34.

21 K. Ren, J. Zhou and H. Wu, Materials for microfluidic chip fabrication, *Acc. Chem. Res.*, 2013, **46**(11), 2396–2406.

22 M. L. Coluccio, G. Perozziello, N. Malara, E. Parrotta, P. Zhang, F. Gentile, T. Limongi, P. Micheal Raj, G. Cuda, P. Candeloro and E. Di Fabrizio, Microfluidic platforms for cell cultures and investigations, *Microelectron. Eng.*, 2019, **208**, 14–28.

23 M. J. Isakson, N. P. Chotiros, R. A. Yarbrough and J. N. Piper, Quantifying the effects of roughness scattering on reflection loss measurements, *J. Acoust. Soc. Am.*, 2012, **132**(6), 3687–3697.

24 L. A. Godwin, K. S. Deal, L. D. Hoepfner, L. A. Jackson and C. J. Easley, Measurement of microchannel fluidic resistance with a standard voltage meter, *Anal. Chim. Acta*, 2013, **758**, 101–107.

25 K. W. Oh, K. Lee, B. Ahn and E. P. Furlani, Design of pressure-driven microfluidic networks using electric circuit analogy, *Lab Chip*, 2012, **12**(3), 515–545.

26 J. Kawai, Chapter 5 - Application of Extended X-Ray Emission Fine Structure Spectroscopy in Soil and Sediments, in *Developments in Soil Science*, ed. B. Singh and M. Gräfe, Elsevier, 2010, vol. 34, pp. 131–146.

27 B. E. Bjärngard and P. Vadash, Relations between scatter factor, quality index and attenuation for X-ray beams, *Phys. Med. Biol.*, 1998, **43**(5), 1325–1330.

28 T. R. Schneider, Synchrotron radiation: micrometer-sized X-ray beams as fine tools for macromolecular crystallography, *HFSP J.*, 2008, **2**(6), 302–306.

29 K. Klementiev, K. Norén, S. Carlson, K. G. V. Sigfridsson Clauss and I. Persson, The BALDER Beamline at the MAX IV Laboratory, *J. Phys.: Conf. Ser.*, 2016, **712**, 012023.

30 I. Persson, D. Lundberg, E. G. Bajnoczi, K. Klementiev, J. Just and K. G. V. Sigfridsson Clauss, EXAFS Study on the Coordination Chemistry of the Solvated Copper(II) Ion in a Series of Oxygen Donor Solvents, *Inorg. Chem.*, 2020, **59**, 9538–9550.

31 S. Reschke, K. G. V. Sigfridsson, P. Kaufmann, N. Leidel, S. Horn, K. Gast, C. Schulzke, M. Haumann and S. Leimkuhler, Identification of a bis-molybdopterin intermediate in molybdenum cofactor biosynthesis in Escherichia coli, *J. Biol. Chem.*, 2013, **288**(41), 29736–29745.

32 H. Dau, P. Liebisch and M. Haumann, X-ray absorption spectroscopy to analyse nuclear geometry and electronic structure of biological metal centers–potential and questions examined with special focus on the tetra-nuclear manganese complex of oxygenic photosynthesis, *Anal. Bioanal. Chem.*, 2003, **376**(5), 562–583.

33 A. L. Ankudinov and J. J. Rehr, Relativistic calculations of spin-dependent X-ray-absorption spectra, *Phys. Rev. B: Condens. Matter Mater. Phys.*, 1997, **56**(4), R1712–R1716.

34 B. Ravel and M. Newville, ATHENA, ARTEMIS, HEPHAESTUS: data analysis for X-ray absorption spectroscopy using IFEFFIT, *J. Synchrotron Radiat.*, 2005, **12**(Pt 4), 537–541.

35 A. Ore, Interaction of ionising radiation with matter, *Mol. Biol., Biochem. Biophys.*, 1978, **27**, 21–30.

36 S. Schweizer, S. Assmann, A. Edgar and J. M. Spaeth, Radiation damage in rare-earth and bromine-doped fluorozirconate glass ceramics as basis for novel X-ray storage phosphors, *Nucl. Instrum. Methods Phys. Res., Sect. B*, 2000, **166–167**, 508–510.

37 C. Li, G. W. Kattawar and P. Yang, Effects of surface roughness on light scattering by small particles, *J. Quant. Spectrosc. Radiat. Transfer*, 2004, **89**(1), 123–131.

38 E. F. Garman and M. Weik, X-ray radiation damage to biological macromolecules: further insights, *J. Synchrotron Radiat.*, 2017, **24**(1), 1–6.

39 G. Bunker, *Introduction to XAFS: A Practical Guide to X-ray Absorption Fine Structure Spectroscopy*, Cambridge University Press, Cambridge, 2010.

40 M. Antalek, E. Pace, B. Hedman, K. O. Hodgson, G. Chillemi, M. Benfatto, R. Sarangi and P. Frank, Solvation structure of the halides from x-ray absorption spectroscopy, *J. Chem. Phys.*, 2016, **145**(4), 044318.

41 W. Levason, J. S. Ogden, M. D. Spicer, M. Webster and N. A. Young, Characterisation of sodium bromite by X-ray crystallography and bromine K-edge EXAFS, IR, Raman, and NMR spectroscopies, *J. Am. Chem. Soc.*, 1989, **111**(16), 6210–6212.